Phase-separated polymer blends for controlled drug delivery by tuning morphology

communications materials

Article

https://doi.org/10.1038/s43246-024-00678-y

Phase-separated polymer blends for controlled drug delivery by tuning morphology

Martina Olsson[1], Robin Storm[2], Linnea Björn[1,3], Viktor Lilja[1], Leonard Krupnik[4,5], Yang Chen[6], Polina Naidjonoka[1], Ana Diaz[6], Mirko Holler[6], Benjamin Watts[6], Anette Larsson[2,3,7], Marianne Liebi[1,6,8] ✉ & Aleksandar Matic[1,3,7] ✉

Controlling drug release rate and providing physical and chemical stability to the active pharmaceutical ingredient are key properties of oral solid dosage forms. Here, we demonstrate a formulation strategy using phase-separated polymer blends where the morphology provides a route for tuning the drug release profile. By utilising phase separation of a hydrophobic and a hydrophilic polymer, the hydrophilic component will act as a channelling agent, creating a porous network upon dissolution that will dictate the release characteristics. With ptychographic X-ray tomography and scanning transmission X-ray microscopy we reveal how the morphology depends on both polymer fraction and presence of drug, and how the drug is distributed over the polymer domains. Combining X-ray imaging results with dissolution studies reveal how the morphologies are correlated with the drug release and showcase how tuning the morphology of a polymer matrix in oral formulations can be utilised as a method for controlled drug release.

The ability to control drug release is important for increased therapeutic effectiveness and patient compliance. Many new drug candidates have poor aqueous solubility and bioavailability, which presents a challenge in pharmaceutical development[1]. Amorphous solid dispersions (ASDs), where the drug is dispersed in a solid carrier matrix with the aim to stabilise the amorphous phase, is a common route to improve the dissolution properties[1]. In addition, the carrier matrix of the ASD can be used to control the release profile, e.g. provide extended release with uniform and prolonged therapeutic effects[2]. Dual polymer-based matrices for ASDs have gained interest for the possibility of combining polymers with different properties[3], e.g. a hydrophobic polymer contributing with physical stability and a hydrophilic polymer providing faster release.

Dual polymer ASDs open opportunities from a processing perspective as they can enable optimisation of flow properties with respect to the requirements of thermal processing[3]. Thermal processing presents several advantages compared to solvent-based methods as it eliminates the risk of toxic residues and costly and unsustainable drying steps of organic solvents[4]. From this perspective, hot melt extrusion (Fig. 1a), has received increased attention in the pharmaceutical industry as a cost-effective and sustainable processing alternative for ASDs[3–5]. In addition, extrusion is a viable pre-step for additive manufacturing, which presents a high potential for advancing personalised medicine in pharmaceutical development.[6]

Phase separation has previously been identified after the extrusion of dual polymer ASDs, but the utilisation for tailored drug release in oral dosage forms has not yet been explored[3]. This study reports on phase-separated polymer blends in solid dispersions as a route for controlled drug release. A phase-separated matrix is created using the hydrophilic polymer, hydroxypropyl methylcellulose (HPMC), and the hydrophobic polymer, polylactic acid (PLA). PLA matrices are commonly used in implants providing extended drug release over several weeks[7], whereas HPMC has a swelling release mechanism and is commonly used in oral controlled release formulations with drug release over the time scale of hours[8]. The combination of these two polymers results in a phase-separated matrix where the hydrophilic HPMC acts as a channelling agent through the PLA matrix,

[1]Department of Physics, Chalmers University of Technology, 41296 Gothenburg, Sweden. [2]Department of Chemistry and Chemical Engineering, Chalmers University of Technology, 41296 Gothenburg, Sweden. [3]Wallenberg Wood Science Centre, Chalmers University of Technology, Gothenburg, 41296, Sweden. [4]Departement Materials meet Life (Empa), Centre for X-ray Analytics, Swiss Federal Laboratories for Materials Science and Technology, 9014 St. Gallen, Switzerland. [5]Department of Chemistry, University of Fribourg, Chemin du Musée 9, 1700 Fribourg, Switzerland. [6]Photon Science Division, Paul Scherrer Institute, 5232 Villigen PSI, Switzerland. [7]Department of Chemistry and Chemical Engineering, FibRe-Centre for Lignocellulose-based Thermoplastics, Chalmers University of Technology, Gothenburg, 41296, Sweden. [8]Institute of Materials, Ecole Polytechnique Fédérale de Lausanne (EPFL), 1015 Lausanne, Switzerland. ✉e-mail: marianne.liebi@psi.ch; matic@chalmers.se

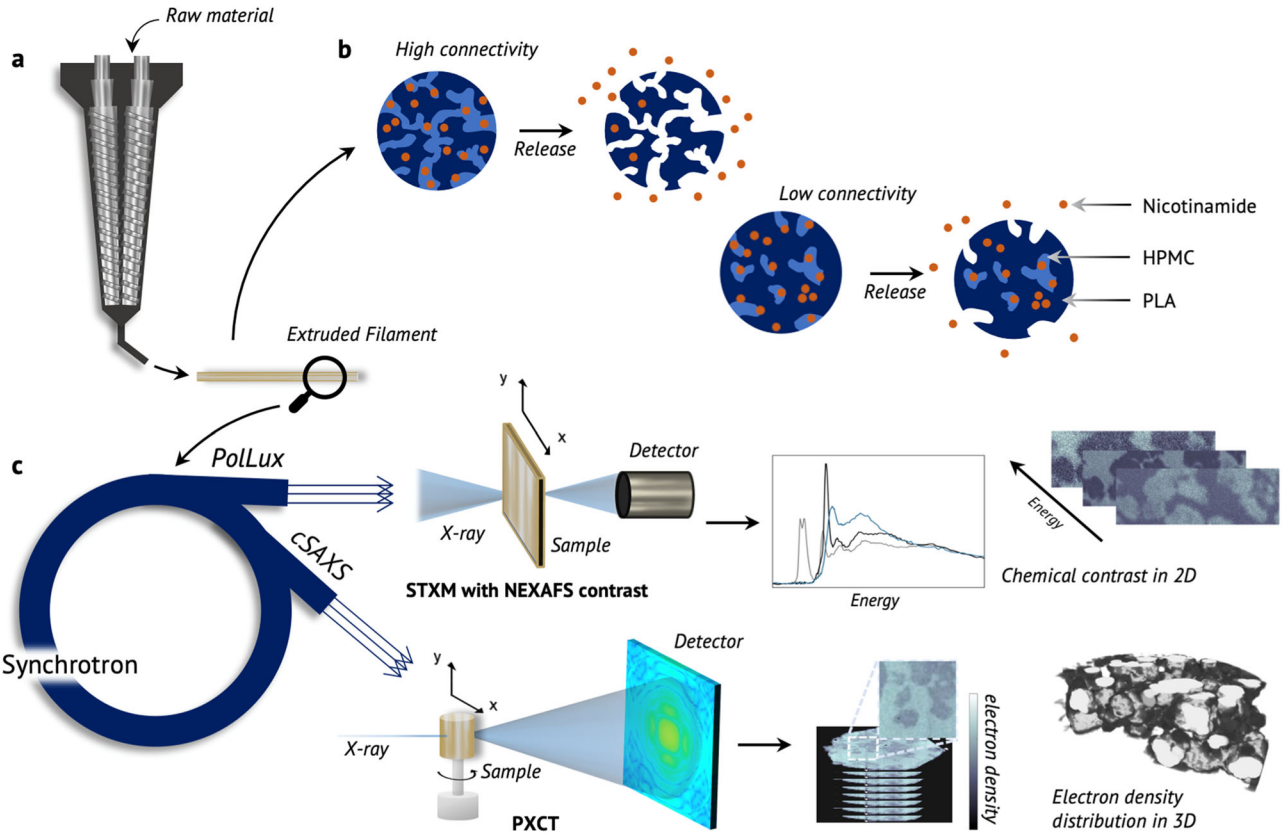

Fig. 1 | Morphological analysis of phase-separated amorphous solid dispersions. **a** Schematic of hot melt extrusion used to create dual polymer ASDs. Polymers and drugs are melt-mixed and forced through a die by the shear forces of the extruder screws, producing a solid filament. **b** Schematic of phase-separated ASDs presenting two scenarios with different morphology. The hydrophobic polymer (dark blue) and the hydrophilic polymer (light blue) phase-separate due to their immiscibility. When exposed to a dissolution medium, the water-soluble phase will dissolve, and the drug (orange) will be released. Two cases of high and low connectivity of the hydrophilic matrix are depicted. In the case of low connectivity, the bulk of the ASD will not be hydrated, and a large fraction of the drug will be trapped and not released. **c** Schematic of the synchrotron X-ray imaging methods and examples of results obtained from them. STXM combines imaging and spectroscopy to generate images with chemical contrast based on the different carbon bonds in the sample. PXCT images the three-dimensional electron density distribution in the sample, and morphological properties such as domain size and connectivity can be retrieved.

illustrated in Fig. 1b, where the connectivity of the phases plays a crucial role in the drug release.

To build a mechanistic understanding of the drug release in phase-separated ASDs, control of the morphology and drug distribution over the two polymers is required. The synchrotron X-ray imaging techniques ptychographic X-ray computed nanotomography (PXCT)[9] and scanning transmission X-ray microscopy (STXM)[10], Fig. 1c, offer a route to access the relevant length scales to image the distribution of polymer and drug. PXCT is a tomography method with high spatial resolution, down to tens of nanometres, and provides the three-dimensional quantitative electron density distribution in an extended volume i.e. $(10–100)^3$ μm^3. The high sensitivity for resolving small electron density differences makes it suitable for characterising phase-separated polymer morphologies[11]. STXM has the advantage of providing chemical contrast by coupling imaging with near-edge X-ray absorption fine structure (NEXAFS) spectroscopy. Tuning the X-ray energies around the carbon K-edge (280–330 eV), images with chemical contrast based on the carbon species are obtained, providing information on the distribution of both polymers and drugs in the ASD, with a resolution of 30 nm within a thin section.

In this work, we demonstrate how the morphology and drug distribution are related to the release profiles of ASDs of 10 wt% nicotinamide in matrices with 30/70, 50/50 and 70/30 PLA/HPMC fractions. Nicotinamide was selected as a model drug for the purpose of the study since it has a high solubility, resulting in dissolution profiles mainly governed by the release kinetics of the polymer blend. The hypothesis for the current system was that the drug release would occur mainly from the HPMC phase as PLA does not erode on the time scale of the dissolution experiment, but rather over multiple weeks[7]. With a low drug load (10 wt%) of a highly soluble drug, the drug release will be governed by the rate of water penetration in the polymer matrix and the diffusion of the drug through the gel layer of the HPMC. It is, therefore, expected that the morphology plays an important role in the dissolution speed as the connectivity will be related to the HPMC phase being wetted, allowing for diffusion of the drug to the dissolution media. The presence of a narrow, tortuous network is expected to reduce the rate of mass transport of water into the polymer matrix as well as for eroded polymer to the dissolution media leading to a decreased drug release rate.

Results and discussion

Physical characterisation and dissolution properties of ASDs

The solid-state form of the drug in the dispersions and the presence of different polymer phases are evaluated using differential scanning calorimetry (DSC) and X-ray diffraction (XRD). DSC reveals that polymer blends without drug show a glass transition, T_g, at ~60 °C and cold crystallisation followed by melting at ~150 °C (Supplementary Figs. 1–3). These are characteristic features of PLA, suggesting that the two polymers phase-separated and create distinct PLA- and HPMC-rich phases. The T_g of HPMC cannot be distinguished in the DSC traces from the polymer blends since it is much weaker compared to the signatures from PLA. In the ASDs with 10 wt% nicotinamide (Fig. 2a), T_g of the PLA-rich phase is found at ~50 °C. This shows that the drug is partly dissolved in the PLA and plasticises the polymer, resulting in a lower T_g[12]. DSC results for dispersions with only PLA and nicotinamide (Supplementary Figs. 4, 5), show that T_g of the

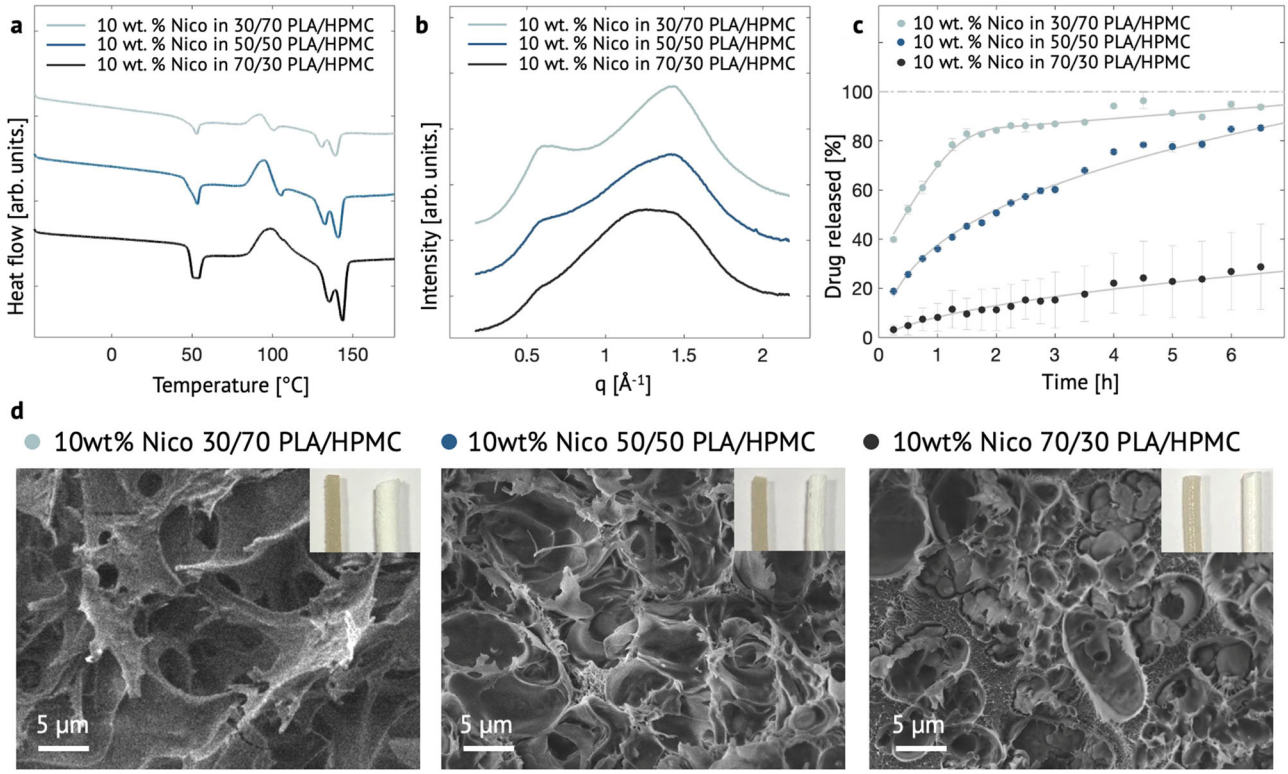

Fig. 2 | Physical characterisation and dissolution profiles of the amorphous solid dispersions. a DSC traces of the ASDs with 10 wt% nicotinamide (Nico) in PLA/HPMC fractions 30/70, 50/50 and 70/30. **b** XRD curves of the ASDs. **c** Dissolution curves of the ASDs. Grey lines are guides to the eye. Error bars represent standard deviations, $n = 2$. **d** SEM images of the remaining polymer matrix after leaching of HPMC. Inset **d** Photographic images of extruded ASD filaments before (left) and after (right) dissolution.

PLA-rich phase in the polymer blend is expected to be around 45 °C if the drug would be equally distributed over the two polymers. The slightly higher T_g (50 °C) found in the ASDs instead suggests that the fraction of nicotinamide in the PLA-rich phase is around 5 wt%, showing that the nicotinamide favours the HPMC. No melting endotherms from crystalline nicotinamide were detected and XRD showed broad peaks characteristic of amorphous systems (Fig. 2b), confirming the stabilisation of amorphous nicotinamide and the formation of an amorphous solid dispersion. At higher drug loading (30 wt%) crystallisation of nicotinamide is observed directly after extrusion, and ASDs could not be successfully obtained.

The drug release profiles of the ASDs were determined by in-vitro dissolution studies, described in the "Methods" section, which show fundamentally different behaviours dependent on PLA/HPMC ratio (Fig. 2c). The dispersion with 30/70 PLA/HPMC displays an initial burst release and most of the drug is released after just 1–2 h. The two dispersions with higher PLA fractions, 50/50 and 70/30 PLA/HPMC, both show slower and more extended-release profiles. In the dispersion with 50/50 PLA/HPMC, the dissolution curve shows a faster initial release that transitions to a slower, linear-like behaviour after the first hour. The 70/30 PLA/HPMC dispersion has a very slow, almost linear release profile, and only 20% of the total drug content is released after 6 h.

Figures 2d and S9 show scanning electron microscopy (SEM) images of the remaining polymer matrix after dissolution for five days, and the insets show photographs of the extruded filaments before (left) and after (right) dissolution. At this point, the HPMC phase can be assumed to be leached, whereas the PLA remains undissolved together with encapsulated nicotinamide and potential HPMC-rich domains, which have not been hydrated due to being completely encapsulated by PLA, as illustrated in Fig. 1b. With a higher fraction of HPMC, the leached filaments are more brittle and porous and disintegrate easily. However, the fact that they are macroscopically cohesive indicates good connectivity of the PLA phase within all dispersions. The volume of the filaments increases during dissolution (Fig. 2d inset), which is a result of the swelling of HPMC upon hydration. The SEM images confirm the porosity created after leaching HPMC. In the dispersions with high HPMC content, 50/50 and 30/70 PLA/HPMC, only thin walls of the insoluble PLA matrix remain, whereas at higher PLA content, 70/30 PLA/HPMC, a denser morphology of the insoluble matrix is observed, also showing a more spherical porosity, which could point to a poorer connectivity of the HPMC phase in this dispersion.

The DSC reveals that the nicotinamide disperses in both polymers. Still, the release profiles show that in the ASDs with a high fraction of HPMC (50/50 and 30/70 PLA/HPMC), most of the drug is released already in the first 6 h of dissolution, whereas PLA normally provides release over multiple weeks. This confirms the preferred partitioning of nicotinamide to the hydrophilic phase, which is a prerequisite for the ASDs to be used in oral extended controlled drug formulations by avoiding a large part of the drug being trapped in the insoluble matrix. However, the large fraction of released drugs in the dissolution study indicates that release also occurs from the PLA in the ASDs. In addition, an increase in T_g of the PLA-rich phase in the leached matrices is found compared to the pristine (Supplementary Figs. 6, 7). This suggests a lower drug concentration after dissolution, supporting that the drug has partly been released from the PLA already within the 5 days of the dissolution experiment. This is in contradiction to the assumption that the PLA would not allow drug release in the formulations on the time scale of our experiment[7]. However, the inferred release from the PLA-rich phase in the phase-separated dispersions can be attributed to the thin skeletal walls remaining after erosion of HPMC (Fig. 2d, Supplementary Fig. 9), exposing a large area of the PLA-rich domains and shorter diffusion paths for the drug to the dissolution medium as a result.

Imaging morphology and drug distribution

To understand how the pristine morphology relates to the extended-release profiles, the ASDs with 10 wt% nicotinamide in 70/30 and 50/50 PLA/HPMC were studied in more detail using STXM and PXCT. Details of

measurements and analysis can be found in the methods. Figure 3 summarises the STXM and NEXAFS results for the characterisation of the two ASDs. Figure 3a displays the carbon K-edge NEXAFS spectra measured for neat PLA, HPMC and nicotinamide. The resonance peaks in NEXAFS spectra correspond to X-ray absorption involving excitations of 1*s* core electrons into unoccupied excited molecular orbitals. Due to the different chemical bonds in the molecules, distinct resonance energies can be used to create an image based on a particular chemical contrast. For instance, nicotinamide shows strong resonance peaks for the C $1s \rightarrow 1\pi^*_{(C=C)/(C=N)}$ transition at 284.4 and 284.9 eV from the aromatic group in the molecule that can be used to map the drug distribution.

Figure 3b shows carbon K-edge NEXAFS spectra taken from the PLA-rich and HPMC-rich domains in the ASD with 10 wt% nicotinamide in 70/30 PLA/HPMC. The two spectra display the characteristic resonances for PLA and HPMC, respectively, as well as resonance peaks from nicotinamide. This confirms the phase separation of the two polymers and that the drug is distributed over both polymer phases. The resonance from nicotinamide in PLA shows the characteristic double peak for the $C1s \rightarrow 1\pi^*_{(C=C)/(C=N)}$ transition, as in neat nicotinamide, while in the spectrum from the HPMC phase, a single resonance peak is found (Fig. 3b inset, Supplementary Fig. 8). Similar changes to energy and intensity distribution of resonance peaks has been observed previously for isonicotinamide in different environments[13] and is suggested to be a consequence of the intermolecular interactions between nicotinamide and HPMC, affecting the conformation and energy of the $C1s \rightarrow 1\pi^*_{(C=C)/(C=N)}$ transition[13,14]. Due to the differences in peak shape in the two polymer phases, direct quantification of nicotinamide content in each phase is not possible, but the signature is used to evaluate the spatial distribution of the drug in the polymer matrix.

Figure 3c and d show the spatial distribution of the three components in a 2D slice of the ASDs with 70/30 PLA/HPMC (Fig. 3c) and 50/50 PLA/HPMC (Fig. 3d). The compositional maps identify the phase-separated HPMC- and PLA-rich domains, and that nicotinamide is present in both phases. From the maps, one can also get the impression that in the 70/30 PLA/HPMC dispersion, the drug favours the HPMC phase, while in 50/50 PLA/HPMC dispersion, the PLA phase is favoured. However, there is a different intensity distribution of the nicotinamide peaks between the two phases, which prevents a direct comparison of the drug concentrations between the two phases. A larger sample thickness of the measured sample in the 50/50 PLA/HPMC also results in a higher uncertainty in the quantitative evaluation of drug partitioning in this sample. Rather than a comparison of the concentration of nicotinamide between the two phases, the results reflect that the drug distribution is homogeneous within each individual phase, down to the length scales of the resolution of the measurement (100 nm). In both samples one bright red spot is observed that can be identified as a small nicotinamide crystal. However, the amount of crystalline nicotinamide in the ASDs is negligible at this composition, as shown with DSC and XRD (Fig. 2).

Figure 3e and f show larger areas of the two dispersions collected at an energy of 288.0 eV, where PLA is highly absorbing and shows up bright, demonstrating a difference in morphology at different polymer fractions. The ASD with 50/50 PLA/HPMC (Fig. 3f) has HPMC-rich domains of a few microns that are relatively homogenous in size and connected throughout the matrix. In contrast, the ASD with 70/30 PLA/HPMC (Fig. 3e) has HPMC-rich domains with various sizes from below one micron up to tens of microns, which shows a lower connectivity through the PLA-rich phase.

Connectivity and local thickness of hydrophilic domains

To further evaluate the different morphologies, PXCT was used to reveal the three-dimensional connectivity of hydrophilic domains. Figure 4 shows the PXCT results for the two ASDs with 10 wt% nicotinamide in 50/50 and 70/30 PLA/HPMC, as well as a polymer blend of 70/30 PLA/HPMC. Figure 4a–c show 2D slices (top-row) from the reconstructed volumes of the three samples. PLA has a slightly higher electron density (0.412 e $Å^{-3}$) compared to HPMC (0.407 e $Å^{-3}$) and shows up bright in the tomograms. These results demonstrate the extraordinary capability of PXCT to resolve small electron density variations, here distinguishing phases with a difference of 0.005 e $Å^{-3}$ in a sample volume of 40*40*20 μm^3. The imaged morphologies are in excellent agreement with what was found in the STXM measurements for the same compositions, Fig. 3d. Figure 4a–c shows 3D volumes of segmented HPMC-rich domains of the three dispersions (bottom-row), illustrated with a colour scheme reflecting the connectivity of

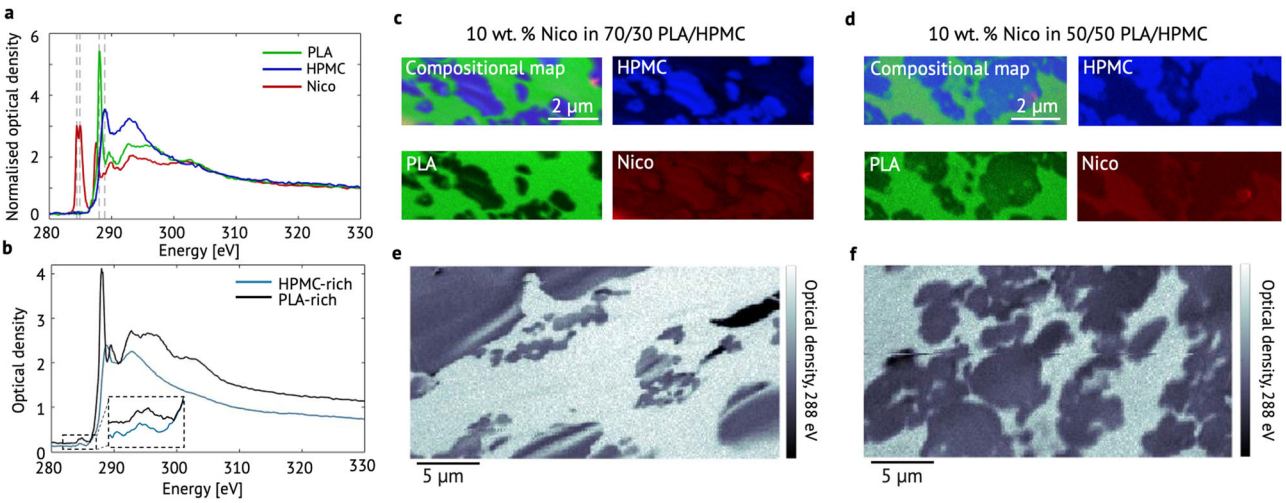

Fig. 3 | Phase distribution evaluated by NEXAFS spectroscopy. a Carbon K-edge NEXAFS spectra for neat PLA, HPMC and nicotinamide. Characteristic resonance energies for each component are marked with dashed lines. The PLA spectrum shows a distinct peak at 288.0 eV characteristic for the $C1s \rightarrow 1\pi^*$(O = C–OR) transition and a peak at 289.5 eV characteristic for the $C1s \rightarrow \sigma^*$ transition for alkyl groups. The HPMC spectrum shows a resonance peak at 288.9 eV and a broad transition at 293 eV for C $1s \rightarrow \sigma^*$ transitions for aliphatic C–OH and aliphatic C–C bonds, characteristic of polysaccharides. The nicotinamide spectrum shows a strong resonance peak for the $C1s \rightarrow 1\ \pi^*_{(C=C)/(C=N)}$ transition at 284.4 and 284.9 eV from the aromatic group in the molecule (**b**) carbon K-edge NEXAFS spectra from PLA- and HPMC-rich domains in 10 wt% nicotinamide in 70/30 PLA/HPMC, demonstrating a difference in peak shape between the polymer domains for the aromatic resonance from nicotinamide (inset, Supplementary Fig. 8). Compositional maps of **c** 10 wt% nicotinamide in 70/30 and **d** 50/50 PLA/HPMC derived from STXM images collected at the resonance energies of the components. STXM images over a more extended region of dispersions with **e** 10 wt% nicotinamide in 70/30 PLA/HPMC and **f** 50/50 PLA/HPMC collected at 288.0 eV where PLA is highly absorbing. PLA-rich domains show up as bright, and HPMC-rich domains as dark domains at this energy.

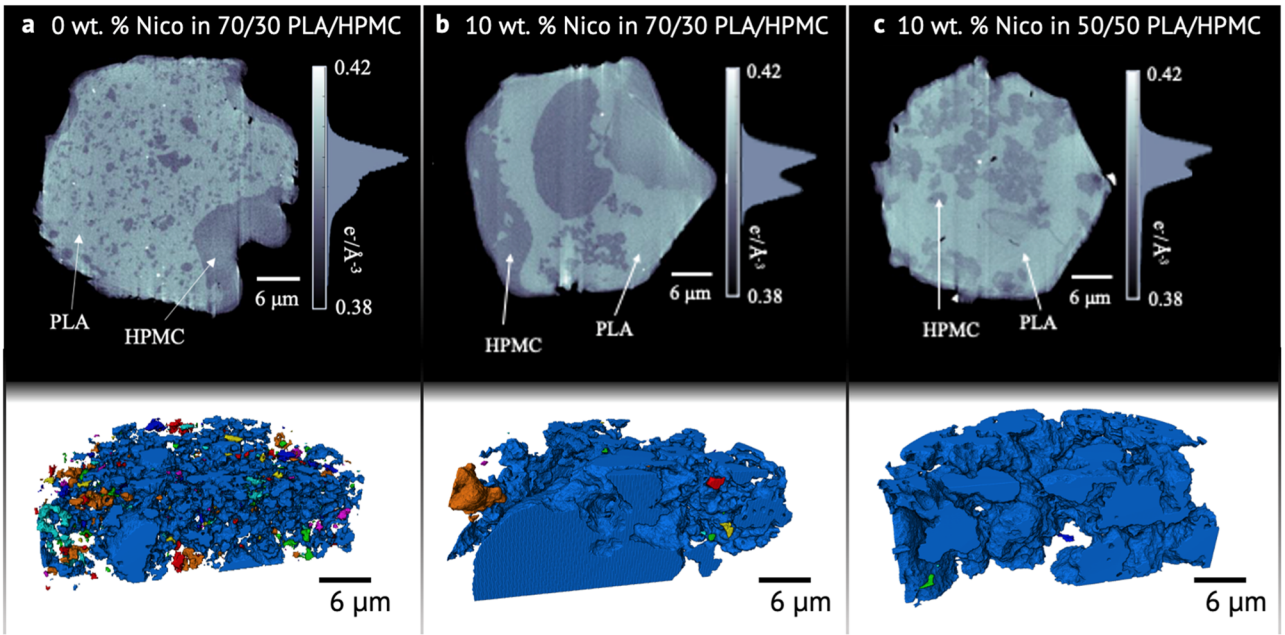

Fig. 4 | Morphology and connectivity of hydrophilic domains. Tomographic slices (top-row) extracted from the reconstructed 3D volumes of **a** 0 wt% and **b** 10 wt% nicotinamide in 70/30 PLA/HPMC and **c** 10 wt% nicotinamide in 50/50 PLA/HPMC. The PLA-rich phase is shown in bright, and the HPMC-rich phase in dark. Grey scale bars indicate quantitative electron density contrast. 3D volume renderings of the segmented HPMC-rich phases (bottom-row), where domains with the same colour are connected, while domains of different colour have no connectivity with other domains in the imaged volume.

hydrophilic domains. Domains with the same colour are connected, while domains of different colours have no connectivity with the rest of the segmented volume. These results show that both ASDs overall have well-connected HPMC-rich domains with small exceptions of domains closer towards the edges, which may be connected outside the imaged volume, and a full hydration of the HPMC-phase is expected in both ASDs during dissolution.

The influence on the morphology of the addition of a drug to the polymer blend can be seen when comparing the morphology of the neat polymer blend to the ASD with polymer fractions 70/30 PLA/HPMC. In the neat polymer blend, Fig. 4a, the HPMC phase is mainly distributed as small microdomains in the PLA matrix, although larger HPMC domains also exist, as seen in the lower right area of the slice. Despite a small average domain size, the HPMC phase has rather high connectivity throughout the imaged volume. With the addition of the drug (Fig. 4b), the HPMC-rich domains become larger, and the size of regions between connected domains increases compared to the polymer blend. These results show that both the size and connectivity of polymer domains are affected by the addition of the drug. This can be attributed to the plasticising effect of the drug[12], which lowers the viscosity of the polymer mixture during extrusion, allowing for the formation of larger, more connected domains.

To further assess the influence of polymer fraction on the morphology of the ASDs, the shape and size distribution of HPMC-rich domains are analysed in detail. Figure 5 shows the results from a local thickness analysis of the HPMC-rich domains in the two ASDs, described in the methods. The local thickness in each pixel is illustrated by a colour, defined by the diameter of the largest sphere that fits inside the domain and contains that pixel. Smaller, narrower, HPMC-rich domains will have a lower local thickness and are coloured in a deeper blue, whereas a bright yellow colour is given to domains of larger local thickness. Figure 5a shows 2D slices from the extracted volumes of segmented HPMC-rich domains, and Fig. 5b the 3D volumes. The histograms in Fig. 5c depict the distribution of local thickness over all pixels in the segmented 3D volumes. The ASD with lower HPMC fraction, (70/30 PLA/HPMC), shows a combination of small narrow domains together with some very large HPMC-rich domains, >7 µm. With increased HPMC fraction, (50/50 PLA/HPMC), a more homogenous distribution of domain thickness is found. By closer inspection of the narrower HPMC-rich domains in the two ASDs, the average local thickness of the smaller domains is lower in the ASD with 70/30 PLA/HPMC (0.85 µm) compared to the ASD with 50/50 PLA/HPMC (1.2 µm). This demonstrates more narrow, tortuous HPMC-rich domains in the dispersion with low HPMC fraction and that the size of the connected regions between hydrophilic domains increases with increased HPMC content. The larger connecting domains in the morphology of the ASD with 50/50 PLA/HPMC fraction allows for efficient penetration of the dissolution medium throughout the dispersion and hence results in a faster dissolution profile compared to the ASD with higher PLA content (Fig. 2c). Conversely, the more narrow, tortuous matrix in the dispersion with 10 wt% nicotinamide in 70/30 PLA/HPMC can be correlated to increasingly extended drug-release profiles of ASDs when the PLA fraction increases.

Comparing the pristine morphology (STXM, PXCT Figs. 3–5) and the leached morphology (SEM, Fig. 2d) demonstrates a distortion of domain structure during dissolution. Whereas the pristine morphology displays a rigid PLA matrix surrounding the HPMC phase, SEM images reveal a fractured structure with only thin walls of PLA remaining in the porous structure after dissolution. This is attributed to the swelling of the hydrophilic polymer, which gets more pronounced in the dispersions with a higher fraction of HPMC. As a result, an increase in the exposed area of the PLA-rich phase and shorter diffusion paths for the drug to the dissolution medium leads to an enhanced drug release from the PLA phase in the dispersions with a high fraction of HPMC. The higher fraction of released drug leads to more efficient use of the drug in the formulation as less drug will be trapped in the insoluble matrix.

In conclusion, our results reveal a correlation between morphology and release rate in phase-separated dispersions. However, it should be noted that the dissolution characteristics of the dispersion will be highly dependent on both composition and selected drug and polymer compounds. The release mechanism will first be dictated by the release characteristics of the polymer and drug species, where morphology can be used as a rate-controlling factor. In the case of a highly soluble drug, as in our work, the release rate is mainly governed by the rate of diffusion of the drug through the wetted HPMC phase. If, instead, a drug with low solubility is used, the release rate is

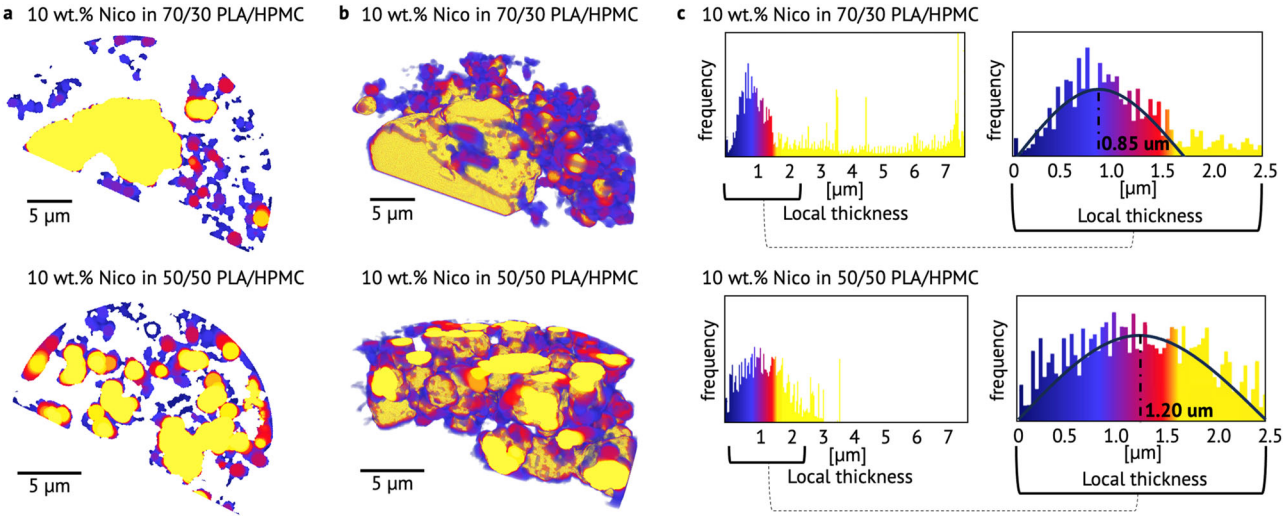

Fig. 5 | Local thickness of hydrophilic domains. Derived local thickness in each pixel in reconstructed **a** 2D slices and **b** 3D volumes of the ASDs with 10 wt% nicotinamide in 70/30 (top row) and 50/50 PLA/HPMC polymer fraction (bottom row). The local thickness in each pixel is illustrated by a colour, defined by the size of the diameter of the largest sphere that fits inside the domain and contains that pixel. **c** Histograms over the local thickness in the volumes illustrated in (**b**).

expected to be dominated by the erosion of the hydrophilic polymer matrix while the drug concentration is kept below the limit of congruency[15].

Prospects for tailoring dissolution profiles with morphological properties in ASDs

Phase-separated polymer blends prepared by hot melt extrusion present a formulation strategy to tailor the drug release of ASDs. In a system with nicotinamide dispersed in hydrophilic HPMC and hydrophobic PLA, the dissolution characteristics are demonstrated to distinctively depend on the polymer ratio. STXM and PXCT reveal that both polymer fraction and the addition of drug affect the morphology in the ASDs, presenting an opportunity to control the drug release profile by the morphology of the phase-separated matrix. With increasing hydrophobic content, a narrower network of hydrophilic polymer domains is created, slowing down the release rate by the slower progression of the dissolution medium through the dispersion. Conversely, the increased fraction of hydrophilic HPMC creates larger connected domains resulting in faster dissolution. By simply adapting the composition of the formulation in the extrusion process, the release profile can be tailored with respect to the intended dissolution, demonstrating the prospects of utilising phase-separated morphologies in ASDs to manufacture pharmaceutical formulations with tailored drug release profiles.

Methods

Preparations of melt-extruded filaments

Nicotinamide (Thermo Fisher, Germany), AFFINISOL HPMC HME 4M (Dow Wollf, Germany) and PLA (NatureWorks LLC, USA) were weighed and physically mixed in a 6 g batch with 0 and 10 wt% nicotinamide in polymer fractions of 30/70, 50/50 and 70/30 PLA/HPMC. The AFFINISOL HPMC HME 4M was selected due to the significantly lower glass transition temperature and melt viscosity as compared to other available grades of HPMC. The mixtures were fed via a hopper into the barrel of a 5 mL capacity Xplore micro compounder with two conical mixing screws and a circular die of ∅ = 1.5 mm. The barrel temperature was set to 180 °C, screw speed of 50 rpm, with a mixing time of 6 min.

Differential scanning calorimetry

A small piece of the sample (~5 mg) was weighed and put in a hermetically sealed aluminium pan. For the DSC measurements, a TA Q1000 instrument was used with helium and nitrogen as purge gases for the sample chamber at a rate of 50 ml/min. The samples were measured by first cooling to −50 °C followed by 1 min isotherm and a heating step to 180 °C, repeated for two cycles. The heating and cooling rates were kept at 10 °C /min. An empty pan was used as a reference.

X-ray diffraction

XRD measurements were carried out using a Mat: Nordic X-ray scattering instrument (SAXSLAB) equipped with a high brilliance Rigaku 003 X-ray micro-focus, Cu-Kα radiation source ($\lambda = 1.5406$ Å) and a Pilatus 300 K detector. Measurements of the dispersions were performed directly over the extruded polymer rods in transmission mode, using an exposure time of 300 s with a sample-to-detector distance of 134 mm, calibrated by LaB6.

Dissolution studies

The dissolution profiles of the ASDs were measured using a USP paddle apparatus (Prolabo, France) with a volume of 900 mL. Phosphate buffer with pH 6.8 was used as a dissolution medium, and a temperature of 37 °C with a paddle speed of 25 RPM was set for the experiment. Two individual dissolution baths for each sample were measured with extruded filaments with a weight of ~100 mg per bath. Each filament had a cylindrical shape with a diameter of ~1.5 mm and a length of 5 cm. For each dissolution curve, duplicate measurements were made. During the first 3 h, a sample was taken every 15 min and after that every 30 min. The samples were left in the buffer for 5 days before being extracted for SEM imaging. The sampled dissolution medium was measured using UV/Vis spectroscopy (Cary 60 UV–Vis, Agilent, USA), and the released nicotinamide concentration was calculated from the absorption peak at 262 nm using a standard curve.

Scanning electron microscopy

SEM imaging of the leached dispersions was performed using a JEOL JSM-7800F Prime microscope with an acceleration voltage of 5 kV. After the dissolution studies, the remaining undissolved matrix of the extruded filaments was quenched in liquid nitrogen and freeze-dried for 24 h to limit structural distortion from water surface tension during drying. The dried filaments were fractured into smaller pieces and sputtered with a 4 nm gold layer prior to the SEM imaging.

Scanning transmission X-ray microscopy

To perform STXM imaging coupled with NEXAFS spectroscopy, the extruded filaments were cut into 150 nm thin sections by an ultramicrotome at room temperature and placed on silicon nitride, Si_3N_4, membranes with a thickness of 100 nm. The STXM/NEXAFS measurements were performed

at the PolLux beamline at the Swiss Light Source, Paul Scherrer Institut (Switzerland)[16]. A 25 nm zone plate was used to focus a monochromatic X-ray beam on the sample and an area of the sample was imaged by raster scanning the sample over the focused beam, collecting the transmission value in each point using a photomultiplier tube (PMT), coupled with a phosphor screen. NEXAFS spectra were acquired by collecting a stack of measurements in the energy range between 280 and 330 eV, covering the carbon K-edge. The step size of the energy scan varied from 0.1 eV around the absorption edge to 1 eV in the post-edge region. STXM images were acquired at selected energies corresponding to resonance energies for the different components in the dispersion with a beam size and step size adapted between 30 and 100 nm depending on the aimed field of view and resolution. Spectral processing was performed using the MANTiS software[17]. The spectra were converted to optical density and spectra and images were normalised by the density of the post-edge measurement to correct for density and thickness variations and emphasise the chemical contrast in the sample. Compositional maps were created by singular value decomposition[18] using the measured reference spectra of the components to obtain images of their spatial distribution.

Ptychographic x-ray computed nanotomography

The extruded filaments were cut and mechanically milled by the lathe system Preppy, developed at the cSAXS beamline[19]. A small part of the extruded filament was glued to an OMNY-pin[20] and ~40 µm-sized pillar was milled from the centre of the extruded strands. The drill was enclosed in a cryogenic chamber cooled by liquid nitrogen to keep the samples from elevated temperatures during milling. The PXCT measurements were performed at the cSAXS beamline (X12SA) at the Swiss Light Source, Paul Scherrer Institut (Switzerland). To mitigate structural changes caused by radiation damage, the measurements were made under cryogenic conditions using the OMNY-setup[21]. A beam with an energy of 6.2 keV was focused on the sample by a coherently illuminated Fresnel zone plate with locally displaced zones, which makes an optimised illumination for ptychography[22]. The beam size on the sample was about 9 µm and ptychographic scans were made with a step size of 1.5 µm to provide an overlap between neighbouring illuminated regions. The diffraction pattern was collected in each scanning position with an acquisition time of 0.05 s by an in-vacuum Eiger 1.5M detector. The detector was placed inside an evacuated flight tube with a sample-to-detector distance of 7.2 m. The ptychographic scans were collected at equally spaced angles from 0° to 180° generating 1600 projections for the tomographic reconstruction. The acquisition was split in two sequentially acquired full tomograms, each with an angular range from 0° to 180°, but with double angular step size. The flux was about 3.5×10^8 photons/s and the total acquisition time for each of the three samples was approximately 10 h, imparting a dose of $\sim 2 \times 10^7$ Gy on the specimen, estimated as the surface dose of the given material composition[23]. To confirm the absence of significant radiation damage, two sub-tomograms of the first and second half of the sampled dataset were reconstructed to confirm the absence of structural differences from the measurement. PtychoShelves and the *cSAXS tomography Matlab package* were used for ptychographic and tomographic reconstructions[24–26]. The ptychographic projections were reconstructed using the difference map algorithm[27] followed by a maximum-likelihood optimisation[28]. The tomographic reconstructions were performed with a filtered back projection algorithm. The half-pitch resolution was determined by Fourier shell correlation to ~100 nm in the tomograms[29].

Image analysis

The reconstructed volumes from PXCT were processed in the software Avizo and ImageJ. Background subtraction was first performed by applying Gaussian blur with a length scale larger than the largest features to remove low-frequency intensity variations. Regions with extensive artefacts were cropped from the volume required to perform a proper segmentation of the volume in two phases. A median filter was applied to reduce high frequency noise and was followed by a watershed-based segmentation of two phases. The segmented HPMC-rich regions were further visualised in Avizo, and a local thickness algorithm was applied in ImageJ to calculate the size of the diameter of the largest sphere that fits inside the object and contains that pixel, generating an estimate of the size of hydrophilic domains in the connected network[30,31].

Data availability

The data reported in this article are available from the corresponding authors upon request.

Received: 23 April 2024; Accepted: 10 October 2024;
Published online: 18 October 2024

References

1. Baghel, S., Cathcart, H., & O'Reilly, N. J. Polymeric amorphous solid dispersions: a review of amorphization, crystallization, stabilization, solid-state characterization, and aqueous solubilization of biopharmaceutical classification system class II drugs. *J. Pharm. Sci.* **105**, 2527–2544 (2016).
2. Tran, P. H.-L., Tran, T. T.-D., Park, J. B. & Lee, B.-J. Controlled release systems containing solid dispersions: strategies and mechanisms. *Pharm. Res.* **28**, 2353–2378 (2011).
3. Hörmann, T. et al. Formulation performance and processability window for manufacturing a dual-polymer amorphous solid dispersion via hot-melt extrusion and strand pelletization. *Int. J. Pharm.* **553**, 408–421 (2018).
4. LaFountaine, J. S., McGinity, J. W. & Williams, R. O. Challenges and strategies in thermal processing of amorphous solid dispersions: a review. *AAPS PharmSciTech* **17**, 43–55 (2016).
5. Tran, P. H., Lee, B.-J. & Tran, T. T. Recent studies on the processes and formulation impacts in the development of solid dispersions by hot-melt extrusion. *Eur. J. Pharm. Biopharm.* **164**, 13–19 (2021).
6. Govender, R., Kissi, E. O., Larsson, A. & Tho, I. Polymers in pharmaceutical additive manufacturing: a balancing act between printability and product performance. *Adv. Drug Deliv. Rev.* **177**, 113923 (2021).
7. Ehtezazi, T. & Washington, C. Controlled release of macromolecules from PLA microspheres: using porous structure topology. *J. Control. Release* **68**, 361–372 (2000).
8. Ma, D. et al. Development of a HPMC-based controlled release formulation with hot melt extrusion (HME). *Drug Dev. Ind. Pharm.* **39**, 1070–1083 (2013).
9. Dierolf, M. et al. Ptychographic X-ray computed tomography at the nanoscale. *Nature* **467**, 436–439 (2010).
10. Urquhart, S. G. et al. NEXAFS spectromicroscopy of polymers: overview and quantitative analysis of polyurethane polymers. *J. Electron Spectrosc. Relat. Phenom.* **100**, 119–135 (1999).
11. Olsson, M. et al. Multiscale X-ray imaging and characterisation of pharmaceutical dosage forms. *Int. J. Pharm.* **642**, 123200 (2023).
12. Siepmann, F., Le Brun, V. & Siepmann, J. Drugs acting as plasticizers in polymeric systems: a quantitative treatment. *J. Control. Release* **115**, 298–306 (2006).
13. Edwards, P. T. et al. Determination of H-atom positions in organic crystal structures by NEXAFS combined with density functional theory: a study of two-component systems containing isonicotinamide. *J. Phys. Chem. A* **126**, 2889–2898 (2022).
14. Kolczewski, C. et al. Detailed study of pyridine at the C1*s* and N1*s* ionization thresholds: the influence of the vibrational fine structure. *J. Chem. Phys.* **115**, 6426–6437 (2001).
15. Saboo, S., Mugheirbi, N. A., Zemlyanov, D. Y., Kestur, U. S. & Taylor, L. S. Congruent release of drug and polymer: a "sweet spot" in the dissolution of amorphous solid dispersions. *J. Control. Release* **298**, 68–82 (2019).
16. Raabe, J. et al. PolLux: a new facility for soft x-ray spectromicroscopy at the Swiss Light Source. *Rev. Sci. Instrum.* **79**, 113704 (2008).

17. Lerotic, M., Mak, R., Wirick, S., Meirer, F. & Jacobsen, C. MANTiS: a program for the analysis of X-ray spectromicroscopy data. *J. Synchrotron Radiat.* **21**, 1206–1212 (2014).
18. Koprinarov, I., Hitchcock, A., McCrory, C. & Childs, R. Quantitative mapping of structured polymeric systems using singular value decomposition analysis of soft X-ray images. *J. Phys. Chem. B* **106**, 5358–5364 (2002).
19. Holler, M. et al. A lathe system for micrometre-sized cylindrical sample preparation at room and cryogenic temperatures. *J. Synchrotron Radiat.* **27**, 472–476 (2020).
20. Holler, M. et al. OMNY PIN—a versatile sample holder for tomographic measurements at room and cryogenic temperatures. *Rev. Sci. Instrum.* **88**, 113701 (2017).
21. Holler, M. et al. OMNY—a tOMography Nano crYo stage. *Rev. Sci. Instrum.* **89**, 043706 (2018).
22. Odstrčil, M., Lebugle, M., Guizar-Sicairos, M., David, C. & Holler, M. Towards optimized illumination for high-resolution ptychography. *Opt. Express* **27**, 14981–14997 (2019).
23. Howells, M. R. et al. An assessment of the resolution limitation due to radiation-damage in x-ray diffraction microscopy. *J. Electron Spectrosc. Relat. Phenom.* **170**, 4–12 (2009).
24. Guizar-Sicairos, M. et al. Phase tomography from x-ray coherent diffractive imaging projections. *Opt. Express* **19**, 21345–21357 (2011).
25. Odstrčil, M., Holler, M., Raabe, J. & Guizar-Sicairos, M. Alignment methods for nanotomography with deep subpixel accuracy. *Opt. Express* **27**, 36637–36652 (2019).
26. Wakonig, K. et al. PtychoShelves, a versatile high-level framework for high-performance analysis of ptychographic data. *J. Appl. Crystallogr.* **53**, 574–586 (2020).
27. Thibault, P., Dierolf, M., Bunk, O., Menzel, A. & Pfeiffer, F. Probe retrieval in ptychographic coherent diffractive imaging. *Ultramicroscopy* **109**, 338–343 (2009).
28. Thibault, P. & Guizar-Sicairos, M. Maximum-likelihood refinement for coherent diffractive imaging. *N. J. Phys.* **14**, 063004 (2012).
29. van Heel, M. & Schatz, M. Fourier shell correlation threshold criteria. *J. Struct. Biol.* **151**, 250–262 (2005).
30. Hildebrand, T. & Rüegsegger, P. A new method for the model-independent assessment of thickness in three-dimensional images. *J. Microsc.* **185**, 67–75 (1997).
31. Dougherty, R. & Kunzelmann, K.-H. Computing local thickness of 3D structures with ImageJ. *Microsc. Microanal.* **13**, 1678–1679 (2007).

Acknowledgements

The authors acknowledge the Paul Scherrer Institute, Villigen PSI, Switzerland, for the provision of synchrotron radiation beamtime at the beamlines cSAXS and PolLux of the S.L.S. We gratefully acknowledge Agnieszka Ziolkowska from Umea Centre for Electron Microscopy for assisting with the sample preparation of thin sections for STXM measurements. This work was supported by the Area of Advance Nano at the Chalmers University of Technology through an excellence initiative Ph.D. student position. The project has received funding from the European Union's Horizon 2020 research and innovation programme under grant agreement No. 731019 (EUSMI) for the beamtime at cSAXS at the S.L.S. The PolLux end station was financed by the German Ministerium für Bildung und Forschung (BMBF) through contracts 05K16WED and 05K19WE2.

Author contributions

M.O., A.L., M.L. and A.M. developed the concept of the study. M.O. designed and performed all the experiments. R.S. prepared the materials and performed the dissolution studies together with M.O. M.O., M.L., L.B., L.K., Y.C. and P.N. performed synchrotron experiments, and B.W., A.D. and M.H. assisted for the synchrotron experiments and contributed to discussions regarding analysis of the experimental results. V.L. performed the initial imaging processing and segmentations of the PXCT data. M.O. wrote the first draft of the paper. All authors revised and approved the paper.

Funding

Open access funding provided by Chalmers University of Technology.

Competing interests

The authors declare no competing interests.

Additional information

Supplementary information The online version contains supplementary material available at https://doi.org/10.1038/s43246-024-00678-y.

Correspondence and requests for materials should be addressed to Marianne Liebi or Aleksandar Matic.

Peer review information *Communications Materials thanks* Kaiqing Long and the other, anonymous, reviewer(s) for their contribution to the peer review of this work. Primary Handling Editors: Rona Chandrawati and John Plummer. A peer review file is available.